

An efficient fully Lagrangian solver for modeling wave interaction with oscillating wave energy converter

Chi Zhang^a, Yanji Wei^b, Frederic Dias^c, Xiangyu Hu^{a,*}

^a*Department of Mechanical Engineering, Technical University of Munich, 85748 Garching, Germany*

^b*Aktis Hydraulics BV, Zwolle 8017 JM, Netherland*

^c*School of Mathematics and Statistics, University College Dublin, Belfield, Dublin 4, Ireland*

Abstract

In this paper, we present an efficient, accurate and fully Lagrangian numerical solver for modeling wave interaction with oscillating wave energy converter (OWSC). The key idea is to couple SPHinXsys, an open-source multi-physics library in unified smoothed particle hydrodynamic (SPH) framework, with Simbody which presents an object-oriented Application Programming Interface (API) for multi-body dynamics. More precisely, the wave dynamics and its interaction with OWSC is resolved by Riemann-based weakly-compressible SPH method using SPHinXsys, and the solid-body kinematics is computed by Simbody library. Numerical experiments demonstrate that the proposed solver can accurately predict the wave elevations, flap rotation and wave loading on the flap in comparison with laboratory experiment. In particular, the new solver shows optimized computational performance through CPU cost analysis and comparison with commercial software package ANSYS FLUENT and other SPH-based solvers in literature. Furthermore, a linear damper is applied for imitating the power take-off (PTO) system to study its effects on the hydrodynamics properties of OWSC and efficiency of energy harvesting. In addition, the present solver is used to model extreme wave condition using the focused wave approach to investigate the extreme loads and motions of OWSC under such extreme wave conditions. It worth noting that though the model validation used herein is a bottom hinged oscillating Wave Energy Converter (WEC), the obtained numerical results show promising potential of the proposed solver to future applications in the design of high-performance WECs.

Keywords: Wave energy converter(WEC), Smoothed particle hydrodynamics (SPH), Simbody, Wave-structure interaction, Oscillating wave energy converter (OWSC)

1. Introduction

In the past decades, renewable ocean wave energy has received tremendous worldwide attention thanks to its abundant and dense energy form and in particular, low environmental impact nature. Consequently, various types

of wave energy converters (WECs) have been developed to harvest electrical power from ocean waves [1]. In general, the working principle of the majority falls into four categories, namely, over-topping devices, oscillating water column devices, oscillating bodies and the others, and more details are referred to a comprehensive review [2]. As one of the most promising WECs, the oscillating wave surge converter (OWSC) has demonstrated its energy absorption capability and hydrodynamic performance [3, 4, 5]. The OWSC consists of a surface-piercing flap hinged near the seabed and oscillating back and forth under the interaction with the conforming incident waves.

*Corresponding author.

Email addresses: c.zhang@tum.de (Chi Zhang),
yanji.wei@aktishydraulics.com (Yanji Wei),
frederic.dias@ucd.ie (Frederic Dias), xiangyu.hu@tum.de
(Xiangyu Hu)

The flap's oscillating motion can be converted into electrical energy by pumping high pressure water ashore to drive a hydro-electric turbine [3, 6]. As experimental study of OWSC has the drawbacks of time consuming and economic expensive, numerical study is of great importance for understanding the hydrodynamics property, assessing the power production and optimizing control strategy [4, 7].

Concerning the numerical study of OWSC, a set of mathematical models have been developed in literature [7, 5]. Folley et al. [8] developed a linearized frequency domain model for small seabed-mounted bottom-hinged WECs and they applied a commercial package based on boundary element method (BEM), e.g., WAMIT, for predicting the wave force, radiation damping and added mass. Renzi and Dias [9, 4] proposed a semi-analytical model based on potential flow for three-dimensional modeling of OWSC in channel [9] and open ocean [4]. These models are simple and computationally efficient, and able to correctly predict the hydrodynamics properties of OWSC. However, they are unable to capture non-linear effects due to the notable assumptions of the potential flow theory. The non-linear effects, such as over-topping and slamming, are of great importance for correctly predicting the flap motion as strong wave loads and large amplitude oscillations are expected during its operation. Therefore, Navier-Stokes (NS) CFD mesh-based solvers have been widely applied in modeling of wave interaction with OWSC. Wei et al. [6, 10] used the commercial package ANSYS FLUENT studied the viscous [6] and slamming [10, 11] effects on OWSC. Schmitt et al. [12] applied OpenFOAM toolbox to assess the applicability of Reynolds-averaged NS (RANS) solver for the simulation of OWSC. Mesh-based methods have demonstrated their accuracy in capturing the nonlinear effects, however, they are generally computational expensive as the complex mesh moving occurs during the flap's large oscillating motion.

An alternative approach, meshless methods, such as smoothed particle hydrodynamics (SPH), have gained popularity in the simulation of nonlinear wave dynamics and wave-structure interaction (WSI) in the past decade [13, 14, 15, 16]. As a fully Lagrangian meshless method, SPH method was originally proposed by Lucy [17] and Gingold and Monaghan [18] for astrophysical applications. Since its inception, SPH method has been success-

fully exploited in a broad variety of applications ranging from solid mechanics [19, 20] to fluid dynamics [21, 22] and fluid-structure interactions (FSI) [23, 24, 13, 25, 26]. Thanks its Lagrangian feature, SPH method is particularly well suited for modeling problems involving significantly varying topology and free material surfaces [27, 28]. Recently, SPH method has been extended to simulate wave interaction with WECs. Dias et al. [5, 29, 30] developed an in-house UCD-SPH code based on OpenMP parallelization for modeling wave interaction with OWSC where the flap is considered as a rigid body and its kinematics is resolved directly in SPH framework. Crespo et al. [31] conducted an SPH simulation for wave interaction with oscillating water column converter. Instead of directly computing Newton-Euler equation to capture the kinematics of rigid body in SPH framework, Brito [32] presented a numerical approach by coupling DualSPHysics with Chrono project to study the wave interaction with OWSC. In their work, the mesh-free DualSPHysics implementation is considered for fluid descriptions and Chrono for mechanical systems. Following Ref. [32], Wei et al. [33] presented a similar approach by coupling Chrono with GPUSPH code. Despite of these developments, SPH method still suffers excessive computational efforts for three-dimensional large scale modeling of OWSC. Dias et al. [5] reported that approximated 70h CPU time is taken for 13s physical simulation time with 3.2 million particles on 72 processors of Intel(R) Xeon(R) CPU E5-2620 by using UCD-SPH code. Wei et al. [33] shown that the computational efforts can be reduced to 2h for 2s physical simulation time with 7 million particles with acceleration of graphics processing unit (GPU) on four NVIDIA Tesla K80 GPUs. More recently, Brito et al. [34] reported 105h computational time for 50s physical simulation time with 11.4 million particles with NVIDIA GTX 2080 alongside an Intel Xeon E5 CPU by using DualSPHysics. With the advances in hardware, large-scale SPH modeling of WECs is becoming more and more possible, however, SPH-based solver implemented on conventional central processing units (CPUs) is still in its infancy.

In this paper, we present an efficient, robust and fully Lagrangian numerical solver implemented on CPUs for modeling wave interaction with OWSC. The new solver is based on coupling two open-source libraries, SPHinXsys (<https://github.com/Xiangyu-Hu/SPHinXsys>)

which is a multi-physics library based on SPH method and Simbody (<https://simtk.org/projects/simbody>) which provides a high-performance multi-body physics object-oriented C++ Application Programming Interface (API). SPHinXsys [35, 36] has shown its robustness, accuracy and versatility in modeling fluid dynamics [37], solid mechanics and fluid-structure interaction [24] and multi-physics problems in cardiac function [38]. By coupling SPHinXsys with Simbody, the proposed solver provides an integrative interface for modeling fluid interaction with arbitrarily defined solid, flexible and the combined structures. The new solver is validated by modeling of regular wave interaction with OWSC and comparing the results with experimental data [6] and those in literature [5, 32]. More importantly, the present solver shows great computational performance compared with the commercial software package ANSYS FLUENT [6], UCD-SPH code [5] and other open-source SPH library [34]. Having the validation, a linear damper is applied to imitate the power take-off system to study its effects on the hydrodynamics properties of OWSC and efficiency in energy harvesting. Then, the extreme loads and motions of OWSC under extreme wave conditions are also investigated by modeling extreme wave condition using the focused wave approach.

The remainder of this paper is organized as follows. Section 2 presents Riemann-based SPH method applied in SPHinXsys for modeling fluid dynamics, the principle characteristic for Simbody and the detailed coupling procedure. Numerical validations and applications for modeling wave interaction with OWSC are presented and discussed in Section 3. Concluding remarks are given in Section 4 and all the codes and data-sets accompanying this work are available in repository of SPHinXsys [35] on GitHub at <https://github.com/Xiangyu-Hu/SPHinXsys>.

2. Methods

In this Section, we first briefly summarize the numerical principle characteristics of SPHinXsys whose detailed algorithms and rigorous validations are referred to Refs. [37, 35, 38, 24, 36]. Then, the main characteristics of Simbody library is introduced and the coupling procedure is presented in detail.

2.1. Governing equations

The mass and momentum conservation equations for incompressible fluid can be written in the Lagrangian frame as

$$\begin{cases} \frac{d\rho}{dt} = -\rho \nabla \cdot \mathbf{v} \\ \rho \frac{d\mathbf{v}}{dt} = -\nabla p + \mu \nabla^2 \mathbf{v} + \rho \mathbf{g} \end{cases}, \quad (1)$$

where ρ is the density, \mathbf{v} the velocity, p the pressure, μ the dynamic viscosity, \mathbf{g} the acceleration due to gravity and $\frac{d}{dt} = \frac{\partial}{\partial t} + \mathbf{v} \cdot \nabla$ represents the material derivative. In weakly-compressible SPH (WCSPH) method, the weakly-compressible assumption [21, 39] is introduced for modeling incompressible flow where an artificial isothermal equation of state (EoS)

$$p = c^2(\rho - \rho^0). \quad (2)$$

is used to close Eq. (1). With the weakly-compressible assumption, the density varies around 1% [39] if an artificial sound speed of $c = 10U_{max}$ is employed, with U_{max} being the maximum anticipated flow speed.

2.2. Riemann-based WCSPH method

The SPHinXsys applies the Riemann-based WCSPH method for fluid dynamics where the continuity and momentum equations are discretized as [40, 37]

$$\begin{cases} \frac{d\rho_i}{dt} = 2\rho_i \sum_j \frac{m_j}{\rho_j} (U^* - \mathbf{v}_i \cdot \mathbf{e}_{ij}) \frac{\partial W_{ij}}{\partial r_{ij}} \\ \frac{d\mathbf{v}_i}{dt} = -m_i \sum_j \frac{2P^*}{\rho_i \rho_j} \nabla_i W_{ij} + m_i \sum_j \frac{2\mu}{\rho_i \rho_j} \frac{\mathbf{v}_{ij}}{r_{ij}} \frac{\partial W_{ij}}{\partial r_{ij}} \end{cases}. \quad (3)$$

Here, m is the mass of particle i , $\mathbf{v}_{ij} = \mathbf{v}_i - \mathbf{v}_j$ the relative velocity, $\nabla_i W_{ij}$ represents the gradient of the kernel function $W(|\mathbf{v}_{ij}|, h)$, where $\mathbf{r}_{ij} = \mathbf{r}_i - \mathbf{r}_j$ and h is the smoothing length, with respect to particle i and $\mathbf{e}_{ij} = \mathbf{r}_{ij}/r_{ij}$. Also, U^* and P^* are the solutions of inter-particle one-dimensional Riemann problem constructed along the unit vector pointing from particle i to j . Following the piece-wise constant reconstruction, the initial states of the Riemann problem are identical to those of particles i and j , i.e.,

$$\begin{cases} (\rho_L, U_L, P_L, c_L) = (\rho_i, -\mathbf{v}_i \cdot \mathbf{e}_{ij}, p_i, c_i) \\ (\rho_R, U_R, P_R, c_R) = (\rho_j, -\mathbf{v}_j \cdot \mathbf{e}_{ij}, p_j, c_j) \end{cases}. \quad (4)$$

For solving the one-dimensional Riemann problem, the SPHinXsys applies the low-dissipation Riemann solver

proposed by Zhang et al . [40] where

$$\begin{cases} U^* = \frac{\rho_L c_L U_L + \rho_R c_R U_R + P_L - P_R}{\rho_L c_L + \rho_R c_R} \\ P^* = \frac{\rho_L c_L P_R + \rho_R c_R P_L + \rho_L c_L \rho_R c_R \beta (U_L - U_R)}{\rho_L c_L + \rho_R c_R} \end{cases}, \quad (5)$$

with $\beta = \min(3 \max(U_L - U_R, 0) / \bar{c}, 1)$ denotes the low dissipation limiter [40] and $\bar{c} = (\rho_L c_L + \rho_R c_R) / (\rho_L + \rho_R)$.

For computational efficiency, the dual-criteria time-stepping method is applied for the time integration of fluid. Following Ref. [37], two time-step criteria are defined as the advection criterion Δt_{ad}

$$\Delta t_{ad} = CFL_{ad} \min\left(\frac{h}{|\mathbf{v}|_{max}}, \frac{h^2}{\nu}\right), \quad (6)$$

and the acoustic criterion Δt_{ac}

$$\Delta t_{ac} = CFL_{ac} \frac{h}{c + |\mathbf{v}|_{max}}. \quad (7)$$

Here, $CFL_{ad} = 0.25$, $CFL_{ac} = 0.6$, $|\mathbf{v}|_{max}$ the maximum particle advection velocity in the flow and ν the kinematic viscosity. Accordingly, the advection criterion controls the updating frequency of particle configuration and the acoustic criterion determines the frequency of the pressure relaxation process. More details and validations are referred to Ref. [37].

Also, at the beginning of each advection time step, the density is reinitialized by

$$\rho_i = \max\left(\rho^*, \rho^0 \frac{\sum W_{ij}}{\sum W_{ij}^0}\right), \quad (8)$$

where ρ^* denotes the density before re-initialization and superscript 0 represents the initial reference value.

2.3. Simbody library

As an open-source library licensed under Apache License 2.0, Simbody is distributed in binary form for multiple platforms and presents an object-oriented API to the application programmers who are of interest to handle the modeling and computational aspects of multi-body dynamics. The Simbody can be applied for incorporating robust, high-performance and minimal-coordinate $O(n)$ multi-body dynamics into a variety range of domain-specific end-user applications, for example, it is used by biomechanists in OpenSim, by roboticists in Gazebo,

and by biomolecular researcher in MacroMoleculeBuilder (MMB).

In the top-level architecture, Simbody consists of three primary objects, e.g., System, State and Study as shown in Figure 1. The System object encapsulates of bodies, joints and forces of a model and defines its parameterization. A complete set of values for each of the System's parameters is called a "state" and the response of a System is determined by the state values. A System's compatible State object has the entries for the values of each "state", for example, time, position and velocity. A Study object couples a System and one or more States, and represents a computational experiment intended to reveal something about the System. For example, a simple evaluation Study merely asks the System to evaluate specific quantities, such as the position, using the values taken from a particular State.

2.4. SPHInXsys and Simbody coupling

As mentioned in the previous Section 2.3, an object-oriented C++ API is provided by Simbody and this feature makes its coupling with SPHInXsys straightforward. In the present framework, the hydrodynamic force exerted on the rigid body is computed by SPHInXsys and passed to Simbody to predict the combined translational and rotational motion by solving the Newton-Euler equation. All the kinematic states, e.g., station location, velocity and acceleration, are stored in Simbody and passed back to SPHInXsys for updating the position, velocity and normal of an ensemble of particles belonging to the corresponding rigid body.

In SPHInXsys, all media are modeled as SPH bodies and each body is composed of an ensemble of SPH particles as shown in Figure 2 which represents a typical example of modeling flow induced vibration of a flexible beam attached to a rigid cylinder. In this framework, whole or parts of solid particles can be constrained to characterize the rigid-body dynamics. For example, the cylinder part can be fixed or moving accordingly by solving Newton-Euler equation and the beam part is constrained to the cylinder meanwhile deformed under the interaction with the surrounding flow.

For modeling of fluid-structure interactions, the total force exerted on the structure by the surrounding fluid is

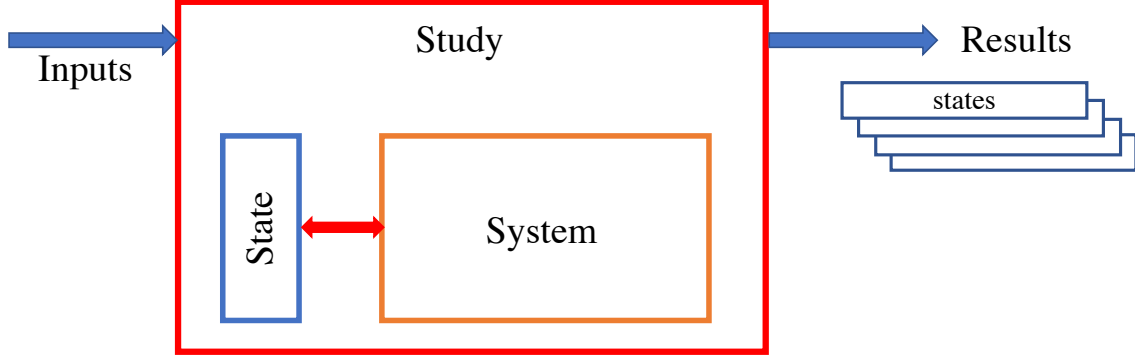


Figure 1: Architecture overview of Simbody. A read-only System object contains the model components and defines the parameterizations. Those parameters' values are stored in State object. The Study object generates a series of states which represent a specific solution.

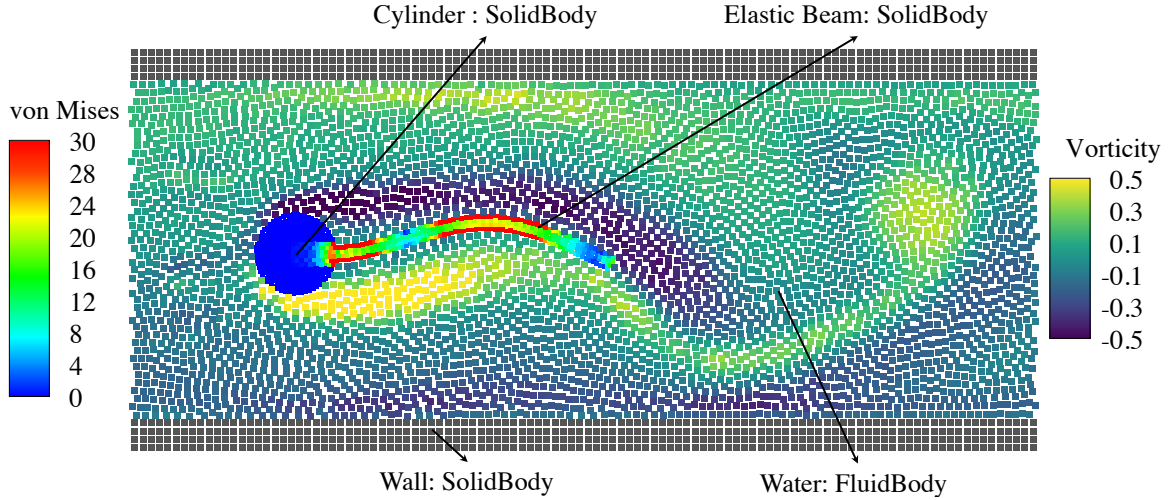


Figure 2: A typical fluid-structure interaction (FSI) involving a rigid solid (wall) body, a composite solid (insert) body and a fluid body. The wall body has two (upper and lower) components. The insert body is composed of a rigid (cylinder) and an elastic (beam) components (For color interpretation, the reader is referred to the web version of this paper).

evaluated through

$$\mathbf{F} = \sum_{a \in N} \mathbf{f}_a, \quad (9)$$

where N is the total particle number for the solid structure and \mathbf{f}_a is calculated through

$$\mathbf{f}_a = -2 \sum_i V_i V_a \frac{p_i \rho_a^d + p_a^d \rho_i}{\rho_i + \rho_a^d} \nabla_a W_{ai} + 2 \sum_i \nu V_i V_a \frac{\mathbf{v}_i - \mathbf{v}_a^d}{r_{ai}} \frac{\partial W_{ai}}{\partial r_{ai}}, \quad (10)$$

where the subscript letter a and i represent particle belong to solid and fluid body, respectively. In Eq. (10), the first and second term in the right-hand-side (RHS) denote the pressure and viscous force, respectively. The imaginary pressure p_a^d and velocity \mathbf{v}_a^d are defined by

$$\begin{cases} p_a^d = p_i + \rho_i \max\left(0, \left(\mathbf{g} - \frac{d\mathbf{v}_a}{dt}\right) \cdot \mathbf{n}\right) (\mathbf{r}_{ai} \cdot \mathbf{n}) \\ \mathbf{v}_a^d = 2\mathbf{v}_i - \mathbf{v}_a \end{cases}, \quad (11)$$

where \mathbf{n} denotes the norm point from solid to fluid. Then,

the total torque acting about the center of mass of the solid body can be expressed as

$$\boldsymbol{\tau} = \sum_{a \in N} (\mathbf{r}_a - \mathbf{r}_{com}) \times \mathbf{f}_a, \quad (12)$$

where \mathbf{r}_{com} is the center of mass. At the end of each fluid time step, the total force and torque are obtained and passed to Simbody for solving the Newton-Euler equation

$$\begin{pmatrix} \mathbf{F} \\ \boldsymbol{\tau} \end{pmatrix} = \begin{pmatrix} m\mathbb{I} & \mathbf{0} \\ \mathbf{0} & \mathbf{I} \end{pmatrix} \begin{pmatrix} \frac{d\mathbf{v}}{dt} \\ \frac{d\boldsymbol{\Omega}}{dt} \end{pmatrix} + \begin{pmatrix} \mathbf{0} \\ -k_d\boldsymbol{\Omega} \end{pmatrix}, \quad (13)$$

where m is the mass of flap, \mathbb{I} the identity matrix, \mathbf{I} the moment of inertia about the center of mass, $\boldsymbol{\Omega}$ is the angular velocity and k_d the damping coefficient. Note that Eq. (13) introduces a linear damper for modeling the PTO damping of OWSC. The detailed coupling procedure are given in the following.

At the beginning of the advection step, the fluid density is reinitialized by Eq. (8) and the viscous force exerted on the solid body is also computed. Then the pressure relaxation process is repeated several times [37] by using the position-based Verlet scheme proposed in Ref. [24]. At first, the integration of the fluid is conducted as

$$\begin{cases} \rho_i^{n+\frac{1}{2}} = \rho_i^n + \frac{1}{2}\Delta t_{ac} \frac{d\rho_i}{dt} \\ \mathbf{r}_i^{n+\frac{1}{2}} = \mathbf{r}_i^n + \frac{1}{2}\Delta t_{ac} \mathbf{v}_i^n \end{cases}, \quad (14)$$

by updating the density and position fields into the mid-point. Then particle velocity is updated to the new time step

$$\mathbf{v}_i^{n+1} = \mathbf{v}_i^n + \Delta t_{ac} \frac{d\mathbf{v}_i}{dt}. \quad (15)$$

Finally, the position and density of fluid particles are updated to the new time step by

$$\begin{cases} \mathbf{r}_i^{n+1} = \mathbf{r}_i^{n+\frac{1}{2}} + \frac{1}{2}\Delta t_{ac} \mathbf{v}_i^{n+1} \\ \rho_i^{n+1} = \rho_i^{n+\frac{1}{2}} + \frac{1}{2}\Delta t_{ac} \frac{d\rho_i}{dt} \end{cases}. \quad (16)$$

At this point, the total pressure force exerted on the solid body is also computed. Now, the total force and torque are obtained and passed to Simbody to solve the Newton-Euler equation and update the State with a Runge-Kutta-Merson integrator. Having the new State, the position, velocity and norm of the whole or parts of solid particles are updated. An overview of the present coupling procedure is shown in Figure 3.

It is worth noting that directly computing Newton-Euler equation to capture the kinematics of rigid body in SPH framework is also feasible and has been implemented in the work of Rafiee et al. [29], Henry et al. [30] and Dias et al. [5]. However, coupling SPHinXsys with Simbody as presented in this work allows us to explore more challenging scenarios, e.g., passive and active flexible fish-like body swimming, wave interaction with elastic structures and flow driven multi-body collisions, which will be explored in the future work.

2.5. Wave making and elimination

In Riemann-base WCSPH, the solid wall boundary can be treated as dummy particle whose interaction with fluid is determined by solving one-sided Riemann problem along the wall-normal direction [40]. Subsequently, the regular wave can be generated by imposing a piston-type wave maker which consists of an ensemble of dummy particles whose displacement is determined by the linear wavemaker theory

$$\mathbf{r}_a = S \sin(ft + \phi), \quad (17)$$

where S is the wave stroke, f the wave frequency and ϕ the initial phase. Here, the wave stroke S is determined by

$$S = \frac{H \sinh(2kh_0) + 2kh_0}{\sinh(2kh_0) \tanh(kh_0)}, \quad (18)$$

where H is the wave height, h_0 the water depth and k is the wave number.

For wave elimination, a damping zone is implemented as passive wave elimination system, where the velocity of the fluid particles reduces at each time step according to their locations in the zone with quadratic decay. Subsequently, the velocity is modified by

$$\mathbf{v} = \mathbf{v}_0 \left(1.0 - \Delta t \alpha \left(\frac{\mathbf{r} - \mathbf{r}_0}{\mathbf{r}_1 - \mathbf{r}_0} \right) \right), \quad (19)$$

where \mathbf{v}_0 denotes the initial velocity of the fluid particle at the entry of the damping zone, \mathbf{v} is the velocity after damping, Δt the time step, \mathbf{r}_0 and \mathbf{r}_1 are the initial and final positions of the damping zone, respectively. Also, the reduction coefficient α controls the modifications on the velocity at each time step and herein we adopt $\alpha = 5.0$.

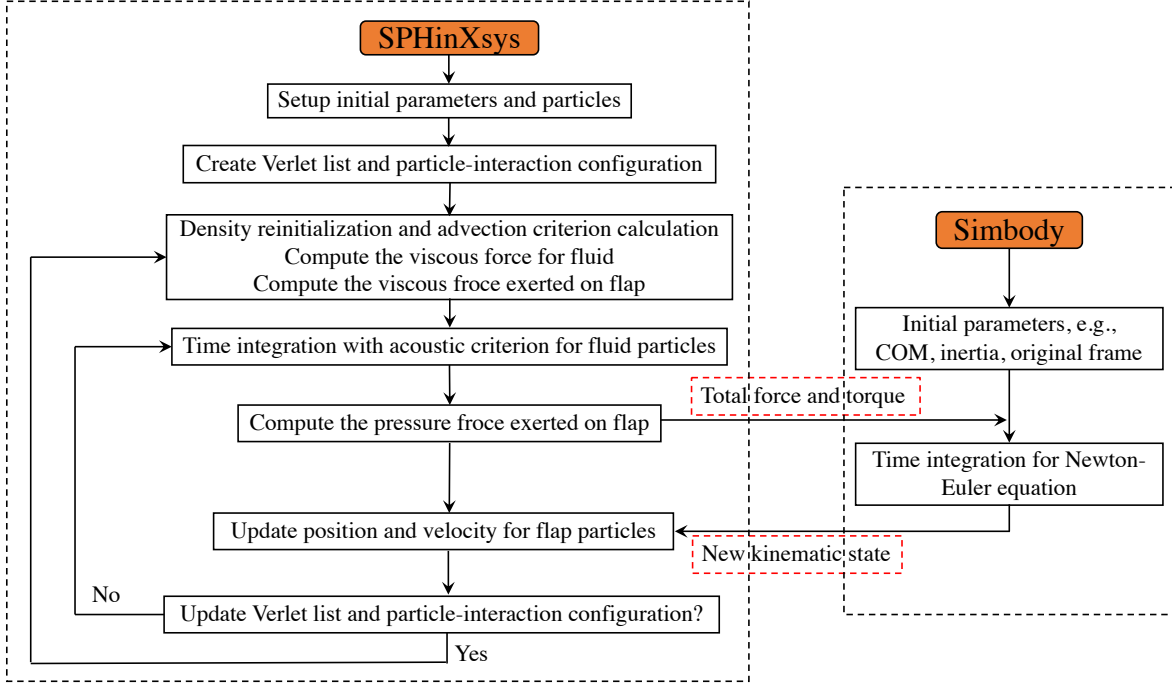


Figure 3: Flow chart of coupling SPHinXsys with Simbody.

3. Modeling of wave interaction with OWSC

In this Section, we present the modeling of wave interaction with OWSC with the proposed numerical solver. We first conduct the validation by comparing the numerical results with experimental data [6] and those in literature [5, 32]. Then, we analyze the computational efficiency by comparing the normalized CPU time with that of ANSYS FLUENT [41], UCD-SPH code [5] and DualSPHysics [34]. Subsequently, the new solver is applied for studying the effects and energy harvesting efficiency of PTO system and extended to investigate the extreme loads on OWSC under extreme wave condition.

3.1. Numerical setup

The present numerical setup is identical to the experiment conducted at the Marine Research Group's hydraulics laboratory at Queen's University Belfast [6]. Following Ref. [6], the numerical wave tank (NWT) is 18.4m long, 4.58m wide and 1.0m high as shown in Figure 4. The OWSC shape is simplified as a $1.04 \times 0.48 \times 0.12\text{m}$

box-type flap which is located 7.92m far from the wave maker in x -axis and in the center of the NWT in z -axis, and hinged to a 0.16m high base. The mass of the flap is 33kg and the inertia of the flap is 1.84kgm^2 . In order to investigate the time variation of the pressure loads, an array of 6 pressure sensors located one side of the front face of the flap (toward the wave maker) is used. The positions of the sensors are given in Table 1 and sensors PS03 and PS11 pierce the initial water free surface. Note that there are 13 pressure sensors in the experiment [6] and herein we choose 6 of them for comparison following the work of Wei et al. [6]. Similarly, three wave probes (there are 14 wave probes in the experiment) were placed in the NWT to elevate the free surface and their locations are given in Table 2. For clarity, the pressure sensors and wave probes are termed identical to those of the experiment. Note that the wave propagates along the x -axis, the y -axis is along the vertical direction (height of the NWT), the flap rotates along the z -axis (width of the NWT) and the rotation angle is positive when the flap pitches land-

ward. Also, the present model is 1 : 25 scale and all the results presented in this paper have been converted to full scale as in Ref. [6].

To discretize the system, the initial particle space is set as $dp = 0.03\text{m}$ resulting in a number of 1.542 million fluid particles and 0.628 million solid particles (including tank, wave maker and flap). The 5th-order Wendland kernel [42] with a smoothing length of $h = 1.3dp$ and a cut-off radius of $2.6dp$ is employed in all the following simulations.

3.2. Model validation

In this Section, we consider the regular wave interaction with OWSC in condition of wave height $H = 5.0\text{m}$ and wave period $T = 10\text{s}$ in full scale. For rigorous and comprehensive validation, comparisons of the main principle aspects of wave-flap interaction, e.g., wave elevation, wave loads on the flap and the flap's rotation, will be conducted same as Ref. [6].

3.2.1. Wave propagation and its interaction with OWSC

Figure 5 presents several snapshots showing the free surface colored by normalized pressure 5a and velocity magnitude 5b, and the flap's rotation predicted by the present solver. It can be observed that smooth pressure and velocity fields are produced even when complex interactions between the wave and the flap are involved. It also worth noting that wave refraction and breaking can be seen in the region near the flap during the interaction. These phenomena can be clearly observed in the time history of the wave elevation presented in the following.

Figure 6 shows the comparison of the present numerical prediction and the laboratory observation [6] for the time histories of the water elevation at probes WP04, WP05 and WP12. For WP04 which is in the seaward of the flap and 3.93m far away from it, a good agreement with the experimental data is noted. For WP05 and WP12 which measure the wave elevation right before and after wave passing the flap, slight discrepancies are noted due to the wave reflection and breaking. It is also interesting to compare the present results with those obtained with ANSYS FLUENT in Ref. [6]. In present work, the wave breaking phenomena are more visible compared with those of FLUENT (see Figure 11 (b) in Ref. [6]) and this is due to the Lagrangian nature of SPH method.

3.2.2. Wave induced rotation of the flap

Figure 7 shows the comparison of the time history of the flap rotation between the present numerical results and the experimental data and also numerical data in literature using SPH-based solver [5, 29, 30, 32], and the corresponding numerical predicted total force on the flap. The comparison in Figure 7a shows that the present solver accurately predicted the large amplitude rotation of the flap implying a robust and stable feature of the coupling between SPHinXsys and Simbody for WSI applications. Compared with results using other SPH-based solver, e.g., UCD-SPH [29, 30, 5] and DualSPHysics [32], the present solver shows improved accuracy in predicting the flap rotation. As noted by Wei et al. [6], the flap's large amplitude rotation is hard to handle by mesh-based methods which require complex mesh technique for moving interface, however, the present solver shows its promising capability of dealing with these difficulties thanks to its very meshless nature.

Figure 7b shows the time history of total force on flap in x - and y -axis. As expected, the force component in x -axis as the main force driving flap rotation shows very similar varying pattern with the rotation profile, on other hand, the y -axis component representing the hydrostatic pressure shows fluctuation due the wave refraction and breaking.

3.2.3. Wave loads on the flap

To optimize the structure design of OWSC, it is also of significant importance to accurately predict the wave loads on its main operating device, e.g., the flap in this study. Figure 8 shows the time histories of the pressure signals recorded on selected sensors given in Table 1 and its comparison with the experimental data [6]. Note that the selected sensors are distributed at the top (PS03 and PS11), middle (PS05 and PS09) and bottom (PS05 and PS13) of the flap. Following Wei et al. [6], the initial hydrostatic pressure is subtracted from the recorded pressure signals inducing a negative drops in some profiles. Compared with the experimental data, the main plateaus of all the pressure profiles are reasonably well captured by the present solver, even if slight discrepancies are noted. For sensors PS01, PS03 and PS11, large pressure peaks and drops are noted since the present SPH model is based on weakly-compressible assumption and air cushion effects are not captured in mono-fluid simulation. Simi-

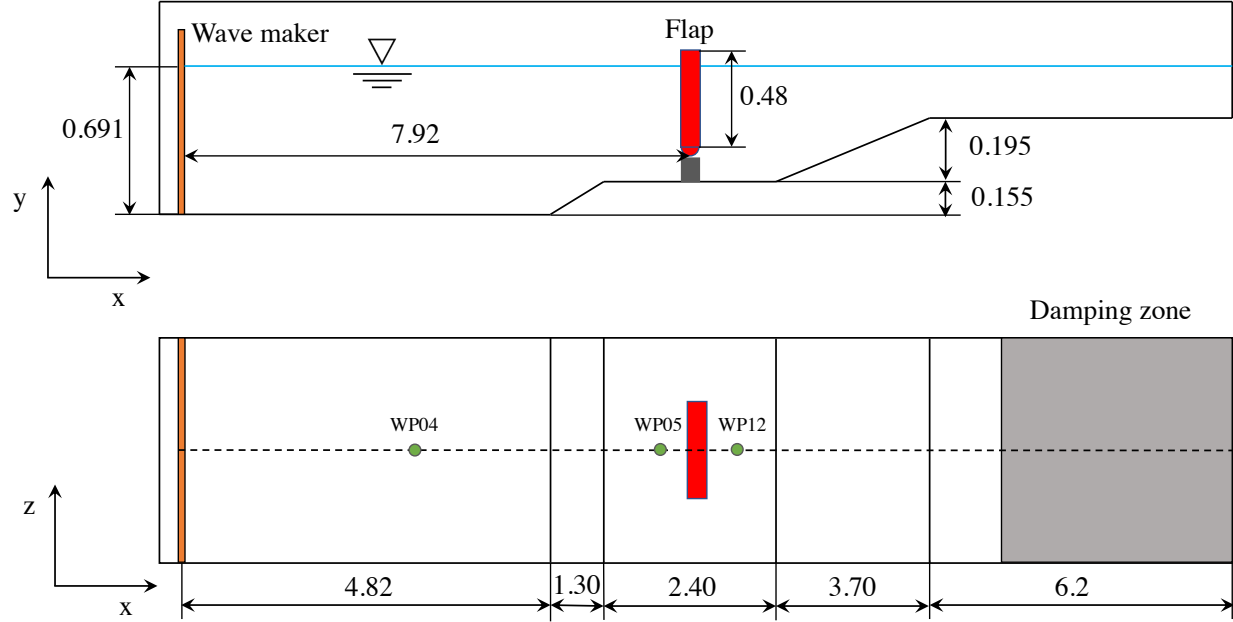


Figure 4: Schematic of the wave tank and the OWSC model. Dimensions are in meters.

Table 1: Positions of the pressure sensors on the front flap face. The position along the z-axis is measured from the center of the device, and $y = 0$ denotes the mean water level.

No.	y-axis (m)	z-axis (m)	No.	y-axis (m)	z-axis (m)
PS01	-0.046	0.468	PS09	-0.117	0.156
PS03	0.050	0.364	PS11	0.025	0.052
PS05	-0.300	0.364	PS13	-0.239	0.052

Table 2: Positions of the wave probes. The position along the z-axis is measured from the center of the device, and $y = 0$ denotes the mean water level.

No.	x-axis (m)	z-axis (m)
WP04	3.99	0
WP05	7.02	0
WP12	8.82	0

lar to the results reported in Ref. [6], the pressure drops for sensors PS05 and PS13 are underestimated in present results and these discrepancies are related to the wave breaking which results in a higher crest elevation compared with experiment as shown in Figure 5. Also note that the-

ses discrepancies are also likely to be associated with the stochastic nature of the impact pressures and the lack of exact repeatability of the experiments.

Compared with the numerical results obtained with ANSYS FLUENT reported in Ref. [6], the present pressure peaks show large magnitudes and fluctuations due to its Lagrangian nature and weakly-compressible assumption. It is worth noting that these large peak magnitudes are not observed in the results obtained by UCD-SPH code [5, 30, 29] and this may be due to the fact that UCD-SPH applied HLLC (Harten Lax and van Leer-Contact) Riemann solver for Riemann-based WCDSPH [43] which induced excessive dissipation [40]. Also, it is interesting to conduct SPH simulation with consideration of air cushion

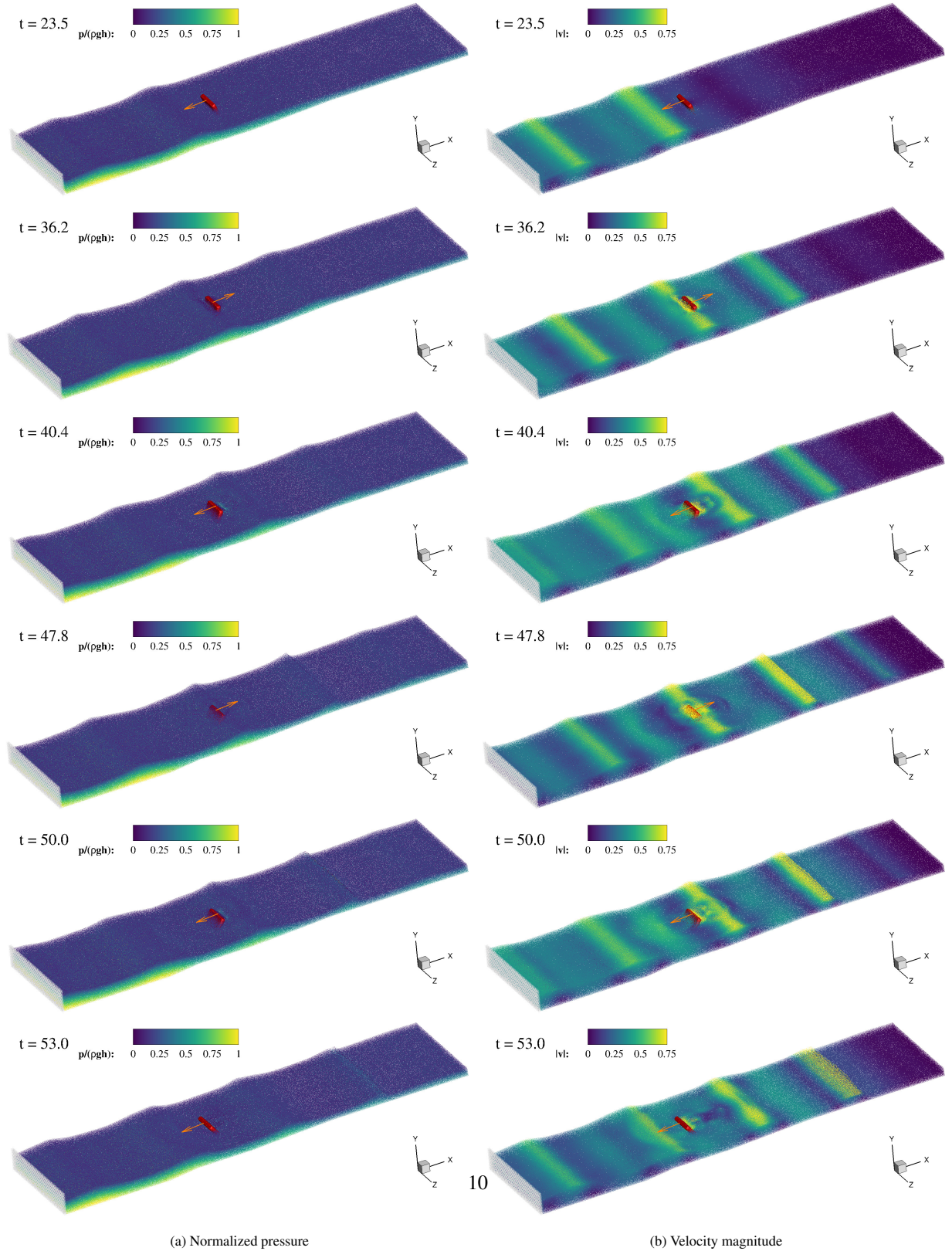


Figure 5: Modeling of OWSC with SPHinXsys: Free surfaces and the flap motion for wave height $H = 5.0\text{m}$ and wave period $T = 10.0\text{s}$. (a) Fluid particles are colored by normalized pressure and (b) fluid particles are colored by velocity magnitude (For color interpretation, the reader is referred to the web version of this paper).

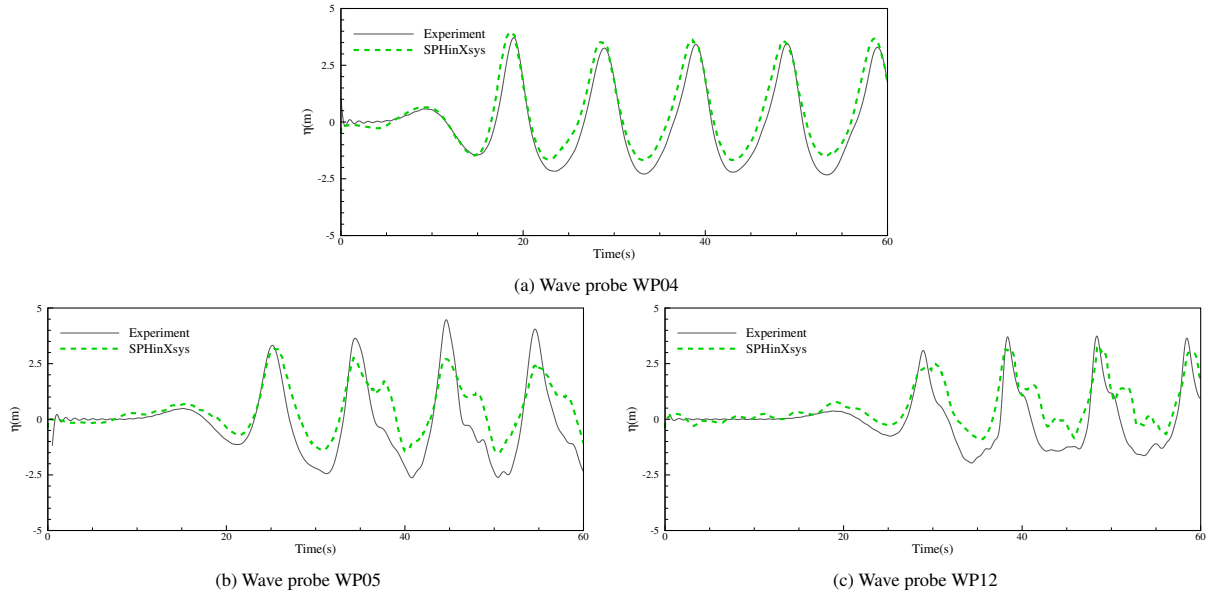


Figure 6: Modeling of OWSC with SPHinXsys: Comparison of free surface elevations for wave height $H = 5.0\text{m}$ and wave period $T = 10.0\text{s}$. The wave probe number : WP04, WP05 and WP12 and their corresponding locations are given in Table 2.

to investigate its effects on pressure peak, and it will be the main objective of our future work.

3.3. Computational efficiency

To rigorously assess the computational performance, we analyze the total CPU time of the present simulation and those or approximated ones reported in literature with different computational models, including commercial software package ANSYS FLUENT [6], in-house UCD-SPH code [29, 5], DualSPHysics [44, 34] and GPUSPH[33]. For comparison, the total CPU time is normalized by total physical time and total cell or particles numbers. The UCD-SPH code was developed by Dias and Rafiee [29, 5] and parallelized based on OpenMP. As for DualSPHysics which is implemented with GPU acceleration, the total CPU time can be approximated by considering the corresponding speedup reported in Ref. [44].

In present work, the computations are carried out on an Intel Xeon CPU E5-2620 v3 2.40GHz Desktop computer with 64GB RAM and Scientific Linux system (7.8). The ANSYS FLUENT and UCD-SPH code are performed on the Stokes cluster of the Irish Centre for High-End Computing (ICHEC) and the Stokes is a SGI Altix ICE

8200EX cluster with 320 compute nodes. Each node has two Intel (Westmere) Xeon E5650 hexa-core processors and 24 GB of RAM and the nodes are interconnected via two planes of ConnectX Infiniband (DDR).

Table 3 reports the computation time and the normalized CPU time with the corresponding physical time, cell or particle number and system information for different models. Although the CPU versions are different, there is no doubt that the present solver shows impressive computational performance for three-dimensional large scale simulations. Also, this performance can be further improved by implementing GPU acceleration which is our ongoing work and will be released soon. Note that as an open-source library, the code and data-sets accompanying this validation is available on the repository of SPHinXsys in GitHub at <https://github.com/Xiangyu-Hu/SPHinXsys>.

ⁱCPU information was not provided for this computation [33], therefore approximated data is not available.

ⁱⁱThe Intel Xeon E5 family is composed of from 4 up to 22 cores.

ⁱⁱⁱNote that the total CPU time for DualSPHysics is approximated by multiplying the 25 speedup with GPU implementation given in Ref.

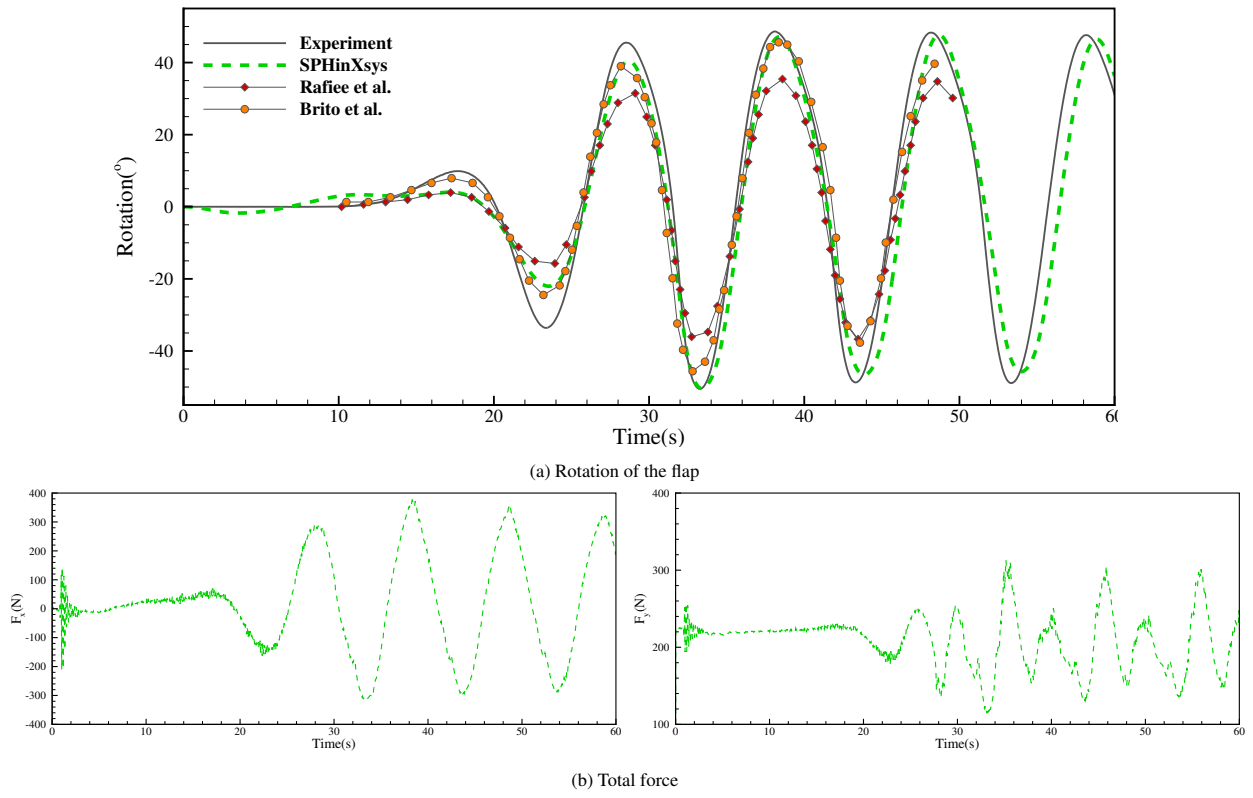


Figure 7: Modeling of OWSC with SPHinXsys: Comparison of the flap rotation (a) and the time histories of the total force exerted on flap in x -axis (left panel of (b)) and y -axis (right panel of (b)).

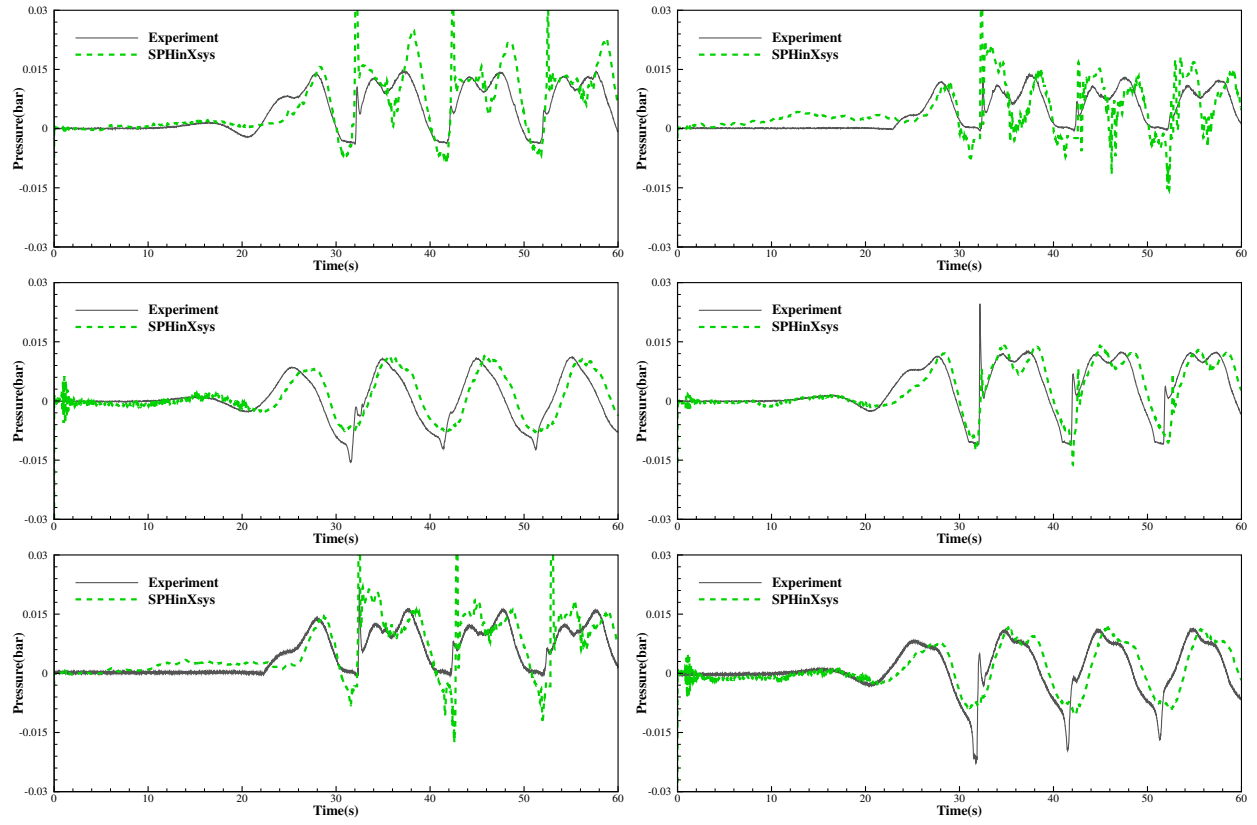


Figure 8: Modeling of OWSC with SPHinXsys: Comparison of the time histories of wave loads on the flap for wave height $H = 5.0\text{m}$ and wave period $T = 10.0\text{s}$. The pressure sensor number (from left to right) : PS01 and PS03 (top panel). PS05 and PS09 (middle panel); PS11 and PS13 (bottom panel).

Table 3: Computational efficiency for different models reported in literature. Here, the CPU time denotes the total CPU time for computation of 1s physical time with 1million particles or cells.

Model	Computing time (hour)	Physical time (s)	Resolution (million)	Device	CPU time (h/s/M)
FLUENT [6]	48h	13s	1.5 M hexahedral cells	24 cores Intel Xeon E5650	59.08
UCD-SPH [5]	70h	13s	3.24 M particles	72 cores Intel Xeon E5650	119.66
GPUSPH [33]	2h	2s	7 M particles	4 GPUs NVIDIA Tesla K80	- ⁱ
DualSPHysics [34]	105h	50s	11.4 M particles	Intel Xeon E5 ⁱⁱ NVIDIA GTX 2080	(0.74 ~ 4.05) × 25 ⁱⁱⁱ
SPHinXsys	8.5h	13s	2.16 M particles	12 Cores Intel Xeon E5-2620	3.63

3.4. Power take-off effects and its energy capture factor

The Simbody provides a linear damper which acts along or around any mobility coordinate to apply a generalized force there which can be applied to imitate the mechanical damping of the PTO operations. In present OWSC model, this process can be defined by Eq. 13 where a damping force proportional to angular velocity is introduced. Note that the damping coefficient k_d represents the extent of kinematic constraint on the flap.

Having the PTO, the efficiency of wave energy harvesting of OWSC can be quantitatively described by the capture factor (CF), which represents the ratio of the power extracted by OWSC to the incident wave power, defined as

$$CF = \frac{P_w}{E_0}, \quad (20)$$

where P_w denotes the time-averaged power extracted by PTO system and E_0 the time-averaged energy flux of incident wave. Following the work of Senol et al. [45], the extracted power P_w can be computed as

$$P_w = \frac{1}{2} \omega^2 k_d |\theta^2|, \quad (21)$$

where ω is the angular frequency of the incident wave, k_d the damping coefficient and θ the rotation amplitude in the pitch component of the flap. Also, the mean energy flux

E_0 is calculated as

$$E_0 = \frac{\rho_0 g \omega H^2}{16k} \left(1 + \frac{2kh_0}{\sinh(2kh_0)} \right) B, \quad (22)$$

where B represents the width of the flap.

Figure 9 shows the time histories of the flap rotation by applying the linear damper with different damping coefficients based on the validated model, e.g., wave height $H = 5.0\text{m}$ and wave period $T = 10.0\text{s}$. As expected, the rotation amplitude is further reduced as the damping coefficient increase. It worth noting that the reduction of the flap rotation does not fit a linear relationship, e.g., the rotation reduction ratio from $k_d = 0$ to $k_d = 20$ is not equal to that from $k_d = 20$ to $k_d = 40$, indicating that the PTO operation may represents a nonlinear process. Figure 10 shows the time histories of the pressure recorded by the pressure sensors given in Table 1 for damping coefficients $k_d = 20$, $k_d = 40$ and $k_d = 80$. One notable phenomenon is that the pressure peaks are reduced or eliminated for pressure sensors PS01, PS03 and PS11 due to the reduced rotation of the flap. This may imply that the strength of the slamming event which leads to the pressure peak [6] is significantly reduced or even eliminated when damping operation is conducted. Also, the pressure drops for sensors PS05, PS09 and PS13 show better agreement with experimental data compared with the results where no damping is imposed. This indicates that wave reflection and breaking are also reduced during damping operations.

Figure 11 gives the variation of the CF in terms of damping coefficients k_d . It can be observed that the CF is

[44].

enhanced as the damping coefficient increase and reaches its maximum about 0.4 when $k_d = 40$, and then shrinks as the damping coefficient further increases, implying that its optimized value of the CF may be achieved for moderate damping coefficient.

3.5. Extreme loads

Prediction of extreme loads on the device of OWSC is of significant importance for the structure design, however, experimental study of the extreme loads is challenging due to its time and economic expensive nature for long time performance of wave tank test. In this work, we apply the present solver to estimate extreme loads on OWSC by considering extreme wave condition based on focused wave approach.

In general, any wave elevation can be considered as the combination of a certain number of small amplitude waves. Therefore, the surface elevation at any point in spatio-temporal spaces can be written as

$$\eta(x, t) = \sum_{i=0}^N a_i \cos(k_i x + \omega_i t + \phi_i), \quad (23)$$

where a_i is the wave amplitude, k_i the wave number, ω the angular frequency and ϕ_i the phase for i th wave component. In the focused wave approach, the phase of each wave component is defined as

$$\phi_i = k_i x_f - \omega_i t_f, \quad (24)$$

where x_f and t_f denote the focal position and time, respectively. The amplitude of each wave component takes the form of

$$a_i = A_f \frac{S(\omega_i) \Delta \omega}{\sum_i S(\omega_i) \Delta \omega}, \quad (25)$$

where A_f is the target amplitude of the focused wave and $S(\omega_i)$ the spectral density. In this work, we apply the Pierson-Moskowitz spectra for modeling the wave spectra and it is given by

$$S(\omega_i) = \frac{5}{16} H_s^2 \omega_p^4 \omega_i^{-5} \exp \left[-\frac{5}{4} \left(\frac{\omega_i}{\omega_p} \right)^{-4} \right], \quad (26)$$

where $H_s = 6.0\text{m}$ and $\omega_p = 2\pi$ are the significant wave height and peak spectra wave angular frequency, respectively.

For piston-type wave maker, the time history of the stroke is given by [46]

$$S_0(t) = \sum_{i=0}^N \frac{a_i}{Tr_i} \sin(k_i x + \omega_i t + \phi_i). \quad (27)$$

Here, the transfer function Tr represents the relationship between the wave height and is given as [47]

$$Tr_i = \frac{2(\cosh(2k_i h_0) - 1)}{\sinh(2k_i h_0) + 2k_i h_0}. \quad (28)$$

Figure 12 shows the time history of the wave elevation at the focused location $x_f = 7.6\text{m}$ and the corresponding flap rotation. As shown in Figure 12a, a sharp wave crest is found at the focused time $t_f = 50\text{s}$ and the amplitude of the surface elevation decreases as the energy content of the wave decrease. Also, wave breaking is noted due to the interaction with the flap. Figure 12b gives the time history of the flap rotation under the interaction with the focused wave. As expected, the sharp wave crest induces a large amplitude rotation of the flap and the amplitude decreases as the wave crest past by.

Figure 13 shows the time histories of the pressure signals recorded on selected sensors given in Table 1 in extreme wave condition. For pressure sensors PS01, PS03 and PS11, which are located close to the surface, a very large pressure peak is observed when the wave crest is impacting on the flap, indicating that a freak wave may induce extreme loads on the flap.

4. Concluding remarks

An efficient, robust and accurate numerical solver is proposed by coupling open-source multi-physics SPH-based library, SPHinXsys, with multi-body physics library, Simbody, for modeling wave interaction with an bottom hinged OWSC.

The proposed numerical solver is validated by comparing the predicted wave elevation, flap rotation and wave loading on the flap with experimental data and those obtained in literature with different numerical models. The comparisons show that the present solver properly predicts the hydrodynamics properties of OWSC. More importantly, optimized computational performance is achieved in the present solver. Then, the validated

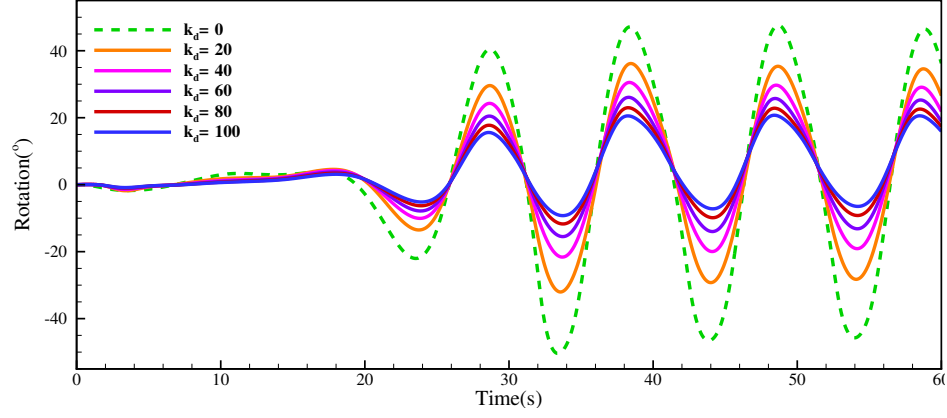


Figure 9: Modeling of OWSC with SPHinXsys: Damping effects on the rotation of the flap for wave height $H = 5.0\text{m}$ and wave period $T = 10.0\text{s}$ (For color interpretation, the reader is referred to the web version of this paper).

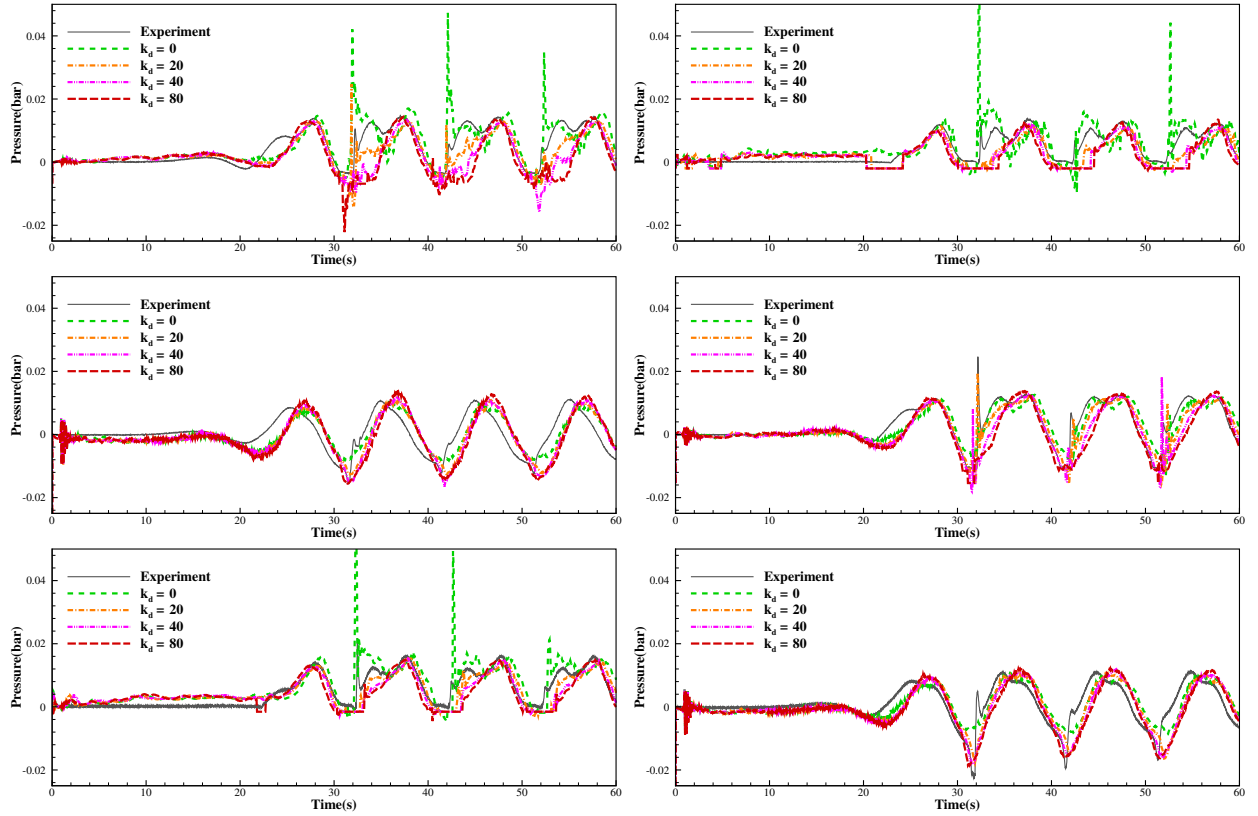


Figure 10: Modeling of OWSC with SPHinXsys: Damping effects on the time history of pressure on the flap for wave height $H = 5.0\text{m}$ and wave period $T = 10.0\text{s}$. The pressure sensor number (from left to right) : PS01 and PS03 (top panel). PS05 and PS09 (middle panel); PS11 and PS13 (bottom panel) (For color interpretation, the reader is referred to the web version of this paper).

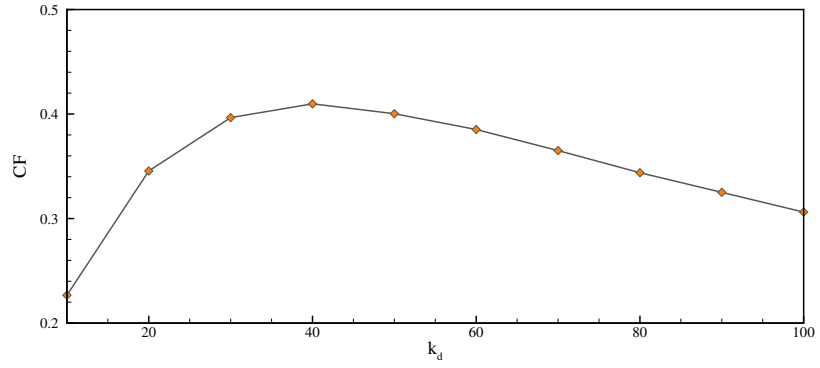


Figure 11: Modeling of OWSC with SPHinXsys: The variations of the CF in terms of damping coefficients for wave height $H = 5.0\text{m}$ and wave period $T = 10.0\text{s}$.

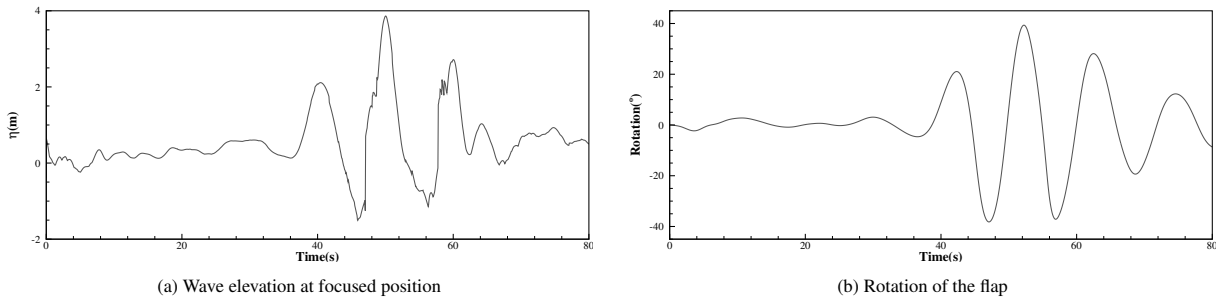


Figure 12: Modeling of OWSC with SPHinXsys: The surface elevation and the corresponding flap rotation under extreme wave condition.

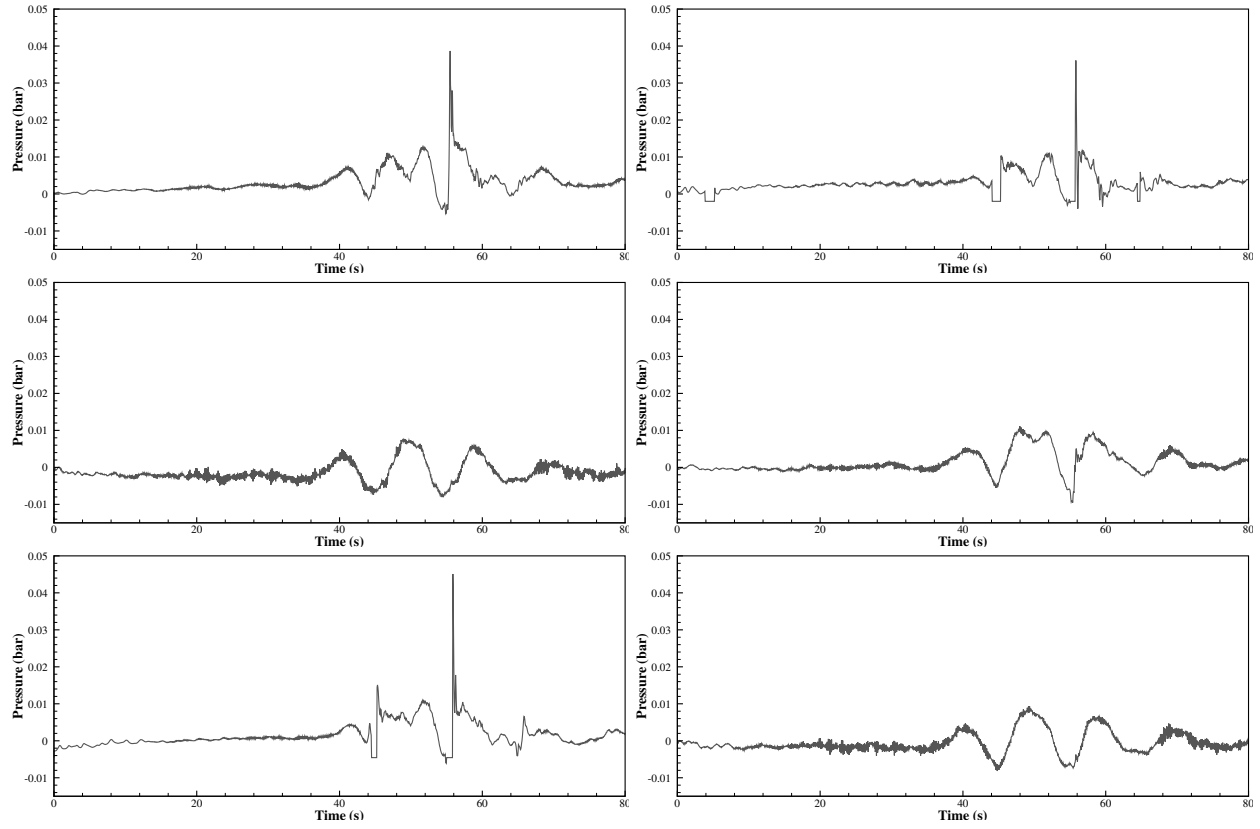


Figure 13: Modeling of OWSC with SPHinXsys: The time histories of wave loads on the flap under extreme wave condition. The pressure sensor number (from left to right) : PS01 and PS03 (top panel). PS05 and PS09 (middle panel); PS11 and PS13 (bottom panel).

solver is applied to study the PTO effects and efficiency, and investigate the extreme loads on the flap in extreme wave conditions. These numerical results demonstrate its promising potential to future practical applications in the design of high-performance WECs.

In future work, GPU implementation will be conducted to further improve the computational efficiency and the slamming effects [10, 11] on OWSC will also be studied.

CRediT authorship contribution statement

Chi Zhang: Investigation, Methodology, Visualization, Validation, Formal analysis, Writing - original draft, Writing - review & editing; **Yanji Wei:** Investigation, Writing - review & editing; **Frederic Dias:** Investigation, Writing - review & editing; **Xiangyu Hu:** Investigation, Supervision, Writing - review & editing.

Declaration of competing interest

The authors declare that they have no known competing financial interests or personal relationships that could have appeared to influence the work reported in this paper.

5. Acknowledgement

C. Zhang and X.Y. Hu would like to express their gratitude to Deutsche Forschungsgemeinschaft (DFG) for their sponsorship of this research under grant numbers DFG HU1527/10-1 and HU1527/12-1. The work of F. Dias has been funded by Science Foundation Ireland (SFI) under Marine Renewable Energy Ireland (MaREI), the SFI Center for Marine Renewable Energy (grant 12/RC/2302).

Reference

References

- [1] A. Day, A. Babarit, A. Fontaine, Y. He, M. Kraskowski, M. Murai, I. Penesis, F. Salvatore, H.-K. Shin, Hydrodynamic modelling of marine renewable energy devices: A state of the art review, *Ocean Engineering* 108 (2015) 46–69.
- [2] F. d. O. Antonio, Wave energy utilization: A review of the technologies, *Renewable and sustainable energy reviews* 14 (3) (2010) 899–918.
- [3] T. Whittaker, D. Collier, M. Folley, M. Osterried, A. Henry, M. Crowley, The development of oyster—a shallow water surging wave energy converter, in: *Proceedings of the 7th European Wave and Tidal Energy Conference*, 2007, pp. 11–14.
- [4] E. Renzi, F. Dias, Hydrodynamics of the oscillating wave surge converter in the open ocean, *European Journal of Mechanics-B/Fluids* 41 (2013) 1–10.
- [5] F. Dias, E. Renzi, S. Gallagher, D. Sarkar, Y. Wei, T. Abadie, C. Cummins, A. Rafiee, Analytical and computational modelling for wave energy systems: the example of oscillating wave surge converters, *Acta Mechanica Sinica* 33 (4) (2017) 647–662.
- [6] Y. Wei, A. Rafiee, A. Henry, F. Dias, Wave interaction with an oscillating wave surge converter, part i: Viscous effects, *Ocean Engineering* 104 (2015) 185–203.
- [7] M. Penalba, G. Giorgi, J. V. Ringwood, Mathematical modelling of wave energy converters: A review of nonlinear approaches, *Renewable and Sustainable Energy Reviews* 78 (2017) 1188–1207.
- [8] M. Folley, T. Whittaker, J. Van't Hoff, The design of small seabed-mounted bottom-hinged wave energy converters, in: *Proceedings of the 7th European wave and tidal energy conference*, Vol. 455, 2007.
- [9] E. Renzi, F. Dias, Resonant behaviour of an oscillating wave energy converter in a channel, *arXiv preprint arXiv:1204.2164* (2012).
- [10] Y. Wei, T. Abadie, A. Henry, F. Dias, Wave interaction with an oscillating wave surge converter. part II: Slamming, *Ocean Engineering* 113 (2016) 319–334.
- [11] F. Dias, J.-M. Ghidaglia, Slamming: Recent progress in the evaluation of impact pressures, *Annual Review of Fluid Mechanics* 50 (2018) 243–273.
- [12] P. Schmitt, B. Elsaesser, On the use of openFOAM to model oscillating wave surge converters, *Ocean Engineering* 108 (2015) 98–104.

- [13] T. Ye, D. Pan, C. Huang, M. Liu, Smoothed particle hydrodynamics (sph) for complex fluid flows: Recent developments in methodology and applications, *Physics of Fluids* 31 (1) (2019) 011301.
- [14] M. Luo, D. E. Reeve, S. Shao, H. Karunarathna, P. Lin, H. Cai, Consistent particle method simulation of solitary wave impinging on and overtopping a seawall, *Engineering Analysis with Boundary Elements* 103 (2019) 160–171.
- [15] M. Luo, C. Koh, Shared-memory parallelization of consistent particle method for violent wave impact problems, *Applied Ocean Research* 69 (2017) 87–99.
- [16] A. Khayyer, H. Gotoh, Y. Shimizu, K. Gotoh, H. Falahaty, S. Shao, Development of a projection-based sph method for numerical wave flume with porous media of variable porosity, *Coastal Engineering* 140 (2018) 1–22.
- [17] L. B. Lucy, A numerical approach to the testing of the fission hypothesis, *The Astronomical Journal* 82 (1977) 1013–1024.
- [18] R. A. Gingold, J. J. Monaghan, Smoothed particle hydrodynamics: theory and application to non-spherical stars, *Mon. Not. R. Astron. Soc.* 181 (3) (1977) 375–389.
- [19] L. D. Libersky, A. G. Petschek, Smooth particle hydrodynamics with strength of materials, in: *Advances in the free-Lagrange method including contributions on adaptive gridding and the smooth particle hydrodynamics method*, Springer, 1991, pp. 248–257.
- [20] J. J. Monaghan, SPH without a tensile instability, *J. Comput. Phys.* 159 (2) (2000) 290–311.
- [21] J. J. Monaghan, Simulating free surface flows with SPH, *J. Comput. Phys.* 110 (2) (1994) 399–406.
- [22] X. Hu, N. Adams, A multi-phase SPH method for macroscopic and mesoscopic flows, *J. Comput. Phys.* 213 (2006) 844–861.
- [23] C. Antoci, M. Gallati, S. Sibilla, Numerical simulation of fluid–structure interaction by SPH, *Computers & Structures* 85 (11–14) (2007) 879–890.
- [24] C. Zhang, M. Rezavand, X. Hu, A multi-resolution SPH method for fluid-structure interactions, *Journal of Computational Physics*, <https://doi.org/10.1016/j.jcp.2020.110028>.
- [25] H. Gotoh, A. Khayyer, On the state-of-the-art of particle methods for coastal and ocean engineering, *Coastal Engineering Journal* 60 (1) (2018) 79–103.
- [26] A. Khayyer, H. Gotoh, et al., Wave impact pressure calculations by improved sph methods, *International Journal of Offshore and Polar Engineering* 19 (04) (2009).
- [27] C. Zhang, X. Y. Hu, N. A. Adams, A generalized transport-velocity formulation for smoothed particle hydrodynamics, *J. Comput. Phys.* 337 (2017) 216–232.
- [28] C. Zhang, G. Xiang, B. Wang, X. Hu, N. Adams, A weakly compressible SPH method with WENO reconstruction, *Journal of Computational Physics* 392 (2019) 1–18.
- [29] A. Rafiee, B. Elsaesser, F. Dias, Numerical simulation of wave interaction with an oscillating wave surge converter, in: *International Conference on Offshore Mechanics and Arctic Engineering*, Vol. 55393, American Society of Mechanical Engineers, 2013, p. V005T06A013.
- [30] A. Henry, P. Schmitt, T. Whittaker, A. Rafiee, F. Dias, et al., The characteristics of wave impacts on an oscillating wave surge converter, in: *The Twenty-third International Offshore and Polar Engineering Conference*, International Society of Offshore and Polar Engineers, 2013.
- [31] A. J. Crespo, M. Hall, J. M. Domínguez, C. Altomare, M. Wu, T. Verbrugge, V. Stratigaki, P. Troch, M. Gómez-Gesteira, Floating moored oscillating water column with meshless SPH method, in: *International Conference on Offshore Mechanics and Arctic Engineering*, Vol. 51333, American Society of Mechanical Engineers, 2018, p. V11BT12A053.

- [32] M. Brito, R. Canelas, R. Ferreira, O. García-Feal, J. Domínguez, A. Crespo, M. Neves, Coupling between dualphysics and chrono-engine: towards large scale hpc multiphysics simulations, in: 11th International SPHERIC Workshop, Munich, Germany, 2016.
- [33] Z. Wei, B. L. Edge, R. A. Dalrymple, A. Hérault, Modeling of wave energy converters by GPUSPH and project chrono, *Ocean Engineering* 183 (2019) 332–349.
- [34] M. Brito, R. Canelas, O. García-Feal, J. Domínguez, A. Crespo, R. Ferreira, M. Neves, L. Teixeira, A numerical tool for modelling oscillating wave surge converter with nonlinear mechanical constraints, *Renewable Energy* 146 (2020) 2024–2043.
- [35] C. Zhang, M. Rezavand, Y. Zhu, Y. Yu, D. Wu, W. Zhang, S. Zhang, J. Wang, X. Hu, SPHinXsys: An open-source meshless, multi-resolution and multi-physics library, *Software Impacts* (2020) 100033.
- [36] C. Zhang, M. Rezavand, Y. Zhu, Y. Yu, D. Wu, W. Zhang, J. Wang, X. Hu, Sphinxsys: an open-source multi-physics and multi-resolution library based on smoothed particle hydrodynamics, *arXiv preprint arXiv:2010.12375* (2020).
- [37] C. Zhang, M. Rezavand, X. Hu, Dual-criteria time stepping for weakly compressible smoothed particle hydrodynamics, *Journal of Computational Physics* 404 (2020) 109135.
- [38] C. Zhang, J. Wang, M. Rezavand, D. Wu, X. Hu, An integrative smoothed particle hydrodynamics framework for modeling cardiac function, *arXiv preprint arXiv:2009.03759* (2020).
- [39] J. P. Morris, P. J. Fox, Y. Zhu, Modeling low reynolds number incompressible flows using SPH, *J. Comput. Phys.* 136 (1) (1997) 214–226.
- [40] C. Zhang, X. Hu, N. A. Adams, A weakly compressible SPH method based on a low-dissipation riemann solver, *J. Comput. Phys.* 335 (2017) 605–620.
- [41] ANSYS, 2012. ANSYS FLUENT 14.0 User’s Guide, ANSYS Inc (2012).
- [42] H. Wendland, Piecewise polynomial, positive definite and compactly supported radial functions of minimal degree, *Adv. Comput. Math.* 4 (1) (1995) 389–396.
- [43] A. Rafiee, S. Cummins, M. Rudman, K. Thiagarajan, Comparative study on the accuracy and stability of sph schemes in simulating energetic free-surface flows, *European Journal of Mechanics-B/Fluids* 36 (2012) 1–16.
- [44] A. J. Crespo, J. M. Domínguez, B. D. Rogers, M. Gómez-Gesteira, S. Longshaw, R. Canelas, R. Vacondio, A. Barreiro, O. García-Feal, DualSPHysics: Open-source parallel CFD solver based on smoothed particle hydrodynamics (SPH), *Computer Physics Communications* 187 (2015) 204–216.
- [45] K. Senol, M. Raessi, Enhancing power extraction in bottom-hinged flap-type wave energy converters through advanced power take-off techniques, *Ocean Engineering* 182 (2019) 248–258.
- [46] D. Ning, J. Zang, S. Liu, R. E. Taylor, B. Teng, P. Taylor, Free-surface evolution and wave kinematics for nonlinear uni-directional focused wave groups, *Ocean Engineering* 36 (15-16) (2009) 1226–1243.
- [47] N. Gao, J. Yang, W. Zhao, X. Li, Numerical simulation of deterministic freak wave sequences and wave-structure interaction, *Ships and Offshore Structures* 11 (8) (2016) 802–817.